The International Journal of Advanced Manufacturing Technology (2024) 133:5553–5570
https://doi.org/10.1007/s00170-024-14079-5

ORIGINAL ARTICLE

A multidisciplinary approach to investigate the influence of process parameters on interlayer adhesion in material extrusion additive manufacturing

Francesco Lambiase[1] · Sara Liparoti[2] · Francesco Pace[1] · Silvia Ilaria Scipioni[1] · Alfonso Paoletti[1]

Received: 5 April 2024 / Accepted: 25 June 2024 / Published online: 4 July 2024

Abstract

This study investigates the influence of deposition conditions in material extrusion (MEX) on fracture toughness, with a specific focus on the interlayer adhesion. A full factorial experimental design was employed, varying three key parameters: the deposition strategy, the extrusion multiplier, and the extruder speed. Fracture toughness was assessed using double cantilever beam tests, following ASTM D5528 standards. Additionally, the study explores the influence of load direction through various deposition strategies, including 0/90 and ± 45 orientations. To gain deeper insights, real-time thermal analysis was conducted during deposition, utilizing an infrared thermal camera. This allowed to investigate the effect of deposition conditions on temperature history. Subsequent examination of fracture surfaces post-testing was performed using optical and scanning electron microscopy. The findings reveal compelling evidence of the significant impact of the extrusion multiplier, printing speed, and deposition orientation on interlayer adhesion. In addition, the results indicated the presence of crystalline phase after deposition which was due to partially melting during depositions involving high material flow. This was due to the adoption of a semicrystalline filament. The adoption of the multidisciplinary approach enabled a better understanding of some phenomena occurring during the deposition (e.g., formation/existence of crystalline phase) that influence the adhesion behavior. These results underline the capability of such broad approach to analyze the influence of the processing conditions on the interlayer adhesion. Consequently, the developed analysis procedure represents a pivotal approach to study and optimize the MEX process and filament characteristics especially for semicrystalline polymers.

Keywords Material extrusion · Fracture toughness · Interlayer adhesion · Deposition conditions · 3D printing, PLA

Abbreviations

a	Pre-crack length
a_0	Initial pre-crack length
b	Specimen width
BT	Beam theory
C	Ratio between the load point displacement and the applied load
DCB	Double cantilever beam
E11	Elastic module along the specimen direction
GIC	Critical energy release rate
IP	Infill percentage
h	Specimen overall thickness
MBT	Modified beam theory
P	Applied load
t	Distance between the loading block and the mid-plane of the first substrate
δ	Machine crosshead displacement
EM	Extrusion multiplier

✉ Francesco Lambiase
francesco.lambiase@univaq.it

[1] Department of Industrial and Information Engineering and Economics, University of L'Aquila, Monteluco Di Roio, Zona Industriale Di Pile, Via G. Gronchi 18, 67100 (AQ) L'Aquila, Italy

[2] Department of Industrial Engineering, University of Salerno, Via Giovanni Paolo II 132, 84084 Salerno, Fisciano, Italy

1 Introduction

Additive manufacturing (AM) is emerging as an innovative and promising technique that could generate finished products or prototypes with intricate geometries while eschewing the limitations imposed by conventional fabrication techniques. The AM techniques provide a wide range of materials and machines, excellent design freedom, and low fixed costs depending on the needs of each application [1, 2].

Material extrusion (MEX) is a flexible subset of the existing AM techniques for making polymer components because of its validated advantages. Polymer filament layers are deposited in a specified repeated pattern to create the final product. These filaments are heated until they either melt; then, they are extruded from a nozzle at that temperature. Recent advancements have made MEX scalable, enabling the production of parts of almost any scale, which aids in fulfilling the requirements for a more comprehensive circular economy. In addition, the MEX process is capable of producing reinforced plastics with short and long fibers to provide higher mechanical behavior [3]. Despite the advantages of these methods, much effort is made into identifying and enhancing the characteristics of AM products related to the processing environment. These parameters primarily relate to the repeatability of the deposition conditions, the reduction of defects like pores and voids, the inadequacy of adhesion between the deposited layers, and shrinkage and warpage connected to the associated heat cycles. Various studies investigated the relationship between the mechanical behavior of AM components and their deposition characteristics [4–12]. The mechanical behavior of MEX parts is greatly influenced by the raster angle, which is created by the direction in which the raster is loaded and deposited [13]. When a load is applied, the raster supports it (raster angle of 0°), and the sample exhibits mechanical characteristics close to the original filament behavior and injection-molded parts [14]. When the load is applied transversely to the raster (at a 90° raster angle), the sample exhibits lower strength and lower elongation at break, which suggests a more brittle nature. Due to this scenario, when the bonded surface between the filaments is loaded, the mechanical properties dramatically decrease. MEX elements consequently show notable anisotropy which can be mitigated by cycling layers with different orientations. However, this approach cannot be successfully employed to improve the mechanical behavior along the building direction (z-direction). Consequently, numerous researchers have been inspired by this to investigate interlayer adhesion using an integrated methodology.

This in turn depends on the thermal history of the adhesion region [15, 16]. In addition, MEX components are intrinsically affected by interlayer voids that develop during deposition, owing to rapid cooling and solidification. This hinders the possibility to achieve full-density components [4], reduces the adhesion area between the layers, and introduces crack initiators. A possible solution to reduce the void dimensions and increase the effective adhesion area between the layers is to increase the extrusion multiplier. In addition, the interfilamentous voids are also strongly influenced by the thermal history. It was proven, through indentation tests, that the filaments built close to the deposition plate show higher adhesion than the filaments built in positions farther from the plate. This behavior was ascribed to the different thermal history experienced by the materials: at the deposition plate, the cooling is delayed allowing for an increase of the rearrangement of the molecules at the interlayer [10]. This was addressed to the prolonged permanence of the material close to the glass transition temperature that enabled higher molecular entanglement, which finally led to higher density. This also led to the enhancement of the mechanical behavior of this region, as described in [17, 18]. Aliheidari et al. [19] investigated mode I fracture toughness tests. Young et al. evaluated the fracture toughness of pure and reinforced ABS specimens [20]. Fonseca et al. [21] examined the interlayer toughness of pure polyamide (PA12) and polyamide reinforced with short fibers. Barile et al. [22] used a double cantilever beam (DCB) specimen to evaluate the mode I fracture toughness of PLA samples. In their study, Khudiakova et al. [23] compared the mode I fracture toughness of PLA versus PLA with carbon reinforcement. Marsavina et al. [24] studied two testing standards made for bulk or composite materials to look at the mode I fracture toughness qualities of PA 2200. Santos et al. [25] performed mode I and mode II fracture toughness tests on 3D printed polyamide/continuous carbon fiber reinforced specimens using ISO and ASTM testing standards.

The SENB testing method, which was just recently established, involves subjecting a straightforward tensile specimen with a notch to cyclic strain [26]. Most of the research employs testing standards for composite materials to evaluate the fracture toughness of additively created parts due to the similarities in mechanical behavior between composite materials and additively generated components. To create the specimen, a film was frequently inserted in the midplane before the pre-crack. However, this requirement may lead to unreliable results, since the time spent for the insertion of the film may alter the thermal history and consequently the adhesion behavior. To this end, Lambiase et al. [27] proposed a new sample that enables to avoid such an artifact. To this end, the authors proposed to use some spacers (directly printed with the same material) at distances of 10 mm to produce the pre-cracks. The spacers were easy to cut leading to pre-crack formation.

Although previous studies have contributed to understand the micromechanics involved during interlayer adhesion, these studies were mainly focused on the fracture analysis and in some cases modeling. In some cases, a few studies investigated the thermal history during the deposition. This strongly influences the interlayer adhesion since it directly impacts the polymeric chain mobility. On the other hand, the interlayer adhesion is also strongly influenced by the formation (or pre-existence) of a crystalline phase that may hinder the mobility of the polymeric chains, and consequently, it could affect the interlayer adhesion.

During the material extrusion process, the formation of interlayer bonding is achieved through molecular

interdiffusion between the material being extruded and the underlying layer. However, different phenomena concur during deposition that makes extremely complex the understanding of the influence of the process parameters on the mechanical behavior. Indeed, the adoption of filaments with high crystalline percentage and process conditions involving high material flow may lead to incomplete melting of the crystalline phase [28, 29]. This could influence negatively the interlayer adhesion. Similarly, deposition conditions have a direct influence on the thermal history, which in turn influences the intermolecular entanglement between overlaying layers. A more comprehensive understanding of these interrelated phenomena occurring during the MEX process requires a broader and interdisciplinary analysis of the process as well as the components made by MEX. Although some investigations were conducted to address the influence of the process parameters on the interlayer adhesion of MEX components, a full understanding of the phenomena involved is still missing. The present study tries to fill this gap by using a multidisciplinary approach involving different methodologies.

Particularly, the aim of this paper is to determine the influence of the deposition strategy, the deposition speed, and the material flow on the interlayer adhesion behavior. PLA was selected as a model material to limit the effect of warpage (more in general, part deformation) and analyze with a multidisciplinary approach the effect of printing conditions to the adhesion. First, experimental tests were conducted by recording thermal imaging through an IR thermal camera to monitor the temperature evolution during the deposition process. This enabled to better investigate the influence of the adopted process parameters on the thermal history. Additionally, extensive physical and chemical characterization were performed to investigate the influence of the involved processing parameters on the interlayer adhesion. Finally, optical and scanning electron microscopy (SEM) were involved to better analyze the fracture surface.

2 Materials and methods

2.1 Materials

PLA filament from (RS PRO 1.75 mm of nominal diameter) was adopted for obtaining the specimens by MEX process. This polymer is characterized by 207.941 g/mol molecular weight, 84.510 g/mol average molecular weight, and 2.461 polydispersity index, as revealed by gas chromatography analysis.

2.2 Design of the DCB specimen

The geometry of the DCB specimen conforms to ASTM D5528 standards. Previous research endeavors [16, 27] have consistently followed this standard, with specific studies focusing on diverse objectives, such as exploring pre-crack introduction methods [27] and investigating the influence of various deposition strategies on the fracture toughness of MEX specimens [16]. This study considers two distinct deposition strategies, resulting in the creation of two types of specimens:

1. 0/90° specimens: These specimens feature a raster angle of 0° in one consecutive layer and 90° in the subsequent layer, as depicted in Fig. 1a.
2. ±45° specimens: These specimens employ a deposition strategy with a ±45° raster angle between consecutive layers, as shown in Fig. 1b.

The adoption of these two deposition strategies facilitates a comprehensive exploration of the influence of raster angle on specimen fracture toughness. This investigation aims to elucidate how different orientations affect mechanical behavior.

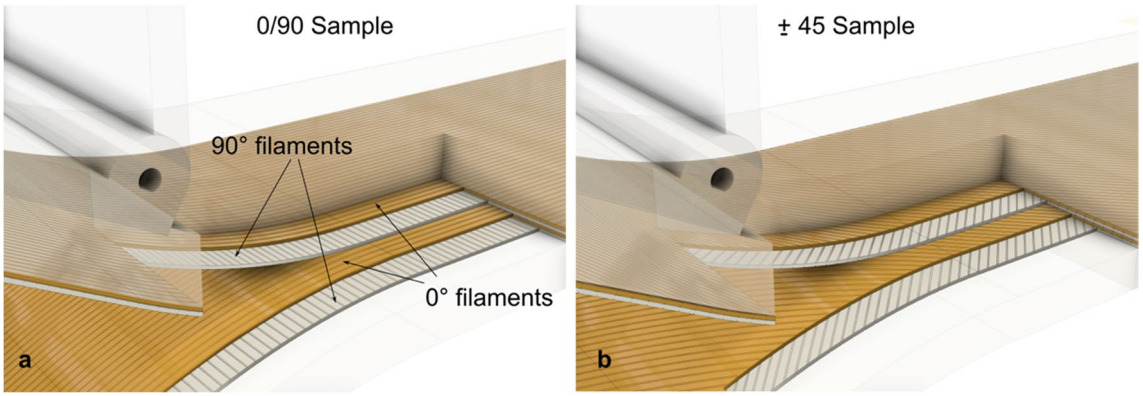

Fig. 1 Relative direction between deposited filaments and applied load and different types of specimens printed via the MEX process: **a** cross-ply specimen (following layers oriented at 0/90°) and **b** angle-ply specimen (following layers oriented at ±45°)

The most important aspect to properly carry out this test is to define the correct geometry of the specimen. The dimensions were identified through the modified beam theory or compliance calibration method according to the corresponding standard. More details concerning the dimensions of the samples are provided in [27].

Tensile tests following ASTM D638 (type 1) were conducted on PLA specimens employing a universal testing machine, specifically the MTS model Criterion 43.50. These tests were performed at a constant speed of 1 mm/min. The outcomes revealed that the longitudinal elastic modulus (E11) values were 2.6 GPa for the ± 45° specimens and 2.7 GPa for the 0/90° specimens. Based on these determined values, the minimum overall thickness was established within the range of 4.5 to 7.5 mm. This dimensional specification was achieved by carefully considering PLA's mechanical properties and adhering to the guidelines outlined in the relevant testing standard ASTM D5528. Table 1 summarizes the dimensions of the samples employed in this study, while Fig. 2 provides a schematic representation of one of these specimens.

2.3 Process parameters and definition of the test matrix

Based on the dimensional specifications, the sample geometry was modeled in 3D using Autodesk Fusion 360 software. A commercial MEX machine model Ender-6 by Creality was used for specimens' fabrication. This machine can be interfaced with the slicer Simplify 3D, which enables to set various parameters of the deposition characteristics. Table 2 provides a summary of the 3D printer parameters that were held constant throughout the various cases in the process.

The layer thickness was fixed at 0.2 mm, equivalent to half the nozzle diameter. Perimeter shells were avoided to eliminate the influence of filaments not aligned with the raster direction. In addition, following the procedure described by Lambiase et al. [27], the pre-crack was produced by printing some thin spacers which can be easily cut, as schematized in Fig. 2b.

Table 3 provides a summary of the test matrix detailing the variations in three key parameters throughout the MEX process:

1. Layer deposition strategy: The study encompassed two deposition strategies, ± 45° and 0/90°, as elucidated in Sect. 2.1.

Table 1 Characteristic dimensions of the specimens used for ASTM D5528 tests

Geometrical characteristics	Dimension (mm)
Length (L)	125
Width (b)	25
Pre-crack length (a)	55
Initial distance of the crack tip from the load axis (a_0)	30

Table 2 **3D** printing parameters employed in all the specimens

Printing parameter	Value
Layer thickness (mm)	0.2
Nozzle diameter (mm)	0.4
Nozzle temperature (°C)	210
Printing bed temperature (°C)	60
Extrusion width (mm)	0.5
Infill percentage (%)	100
Internal fill pattern	Grid

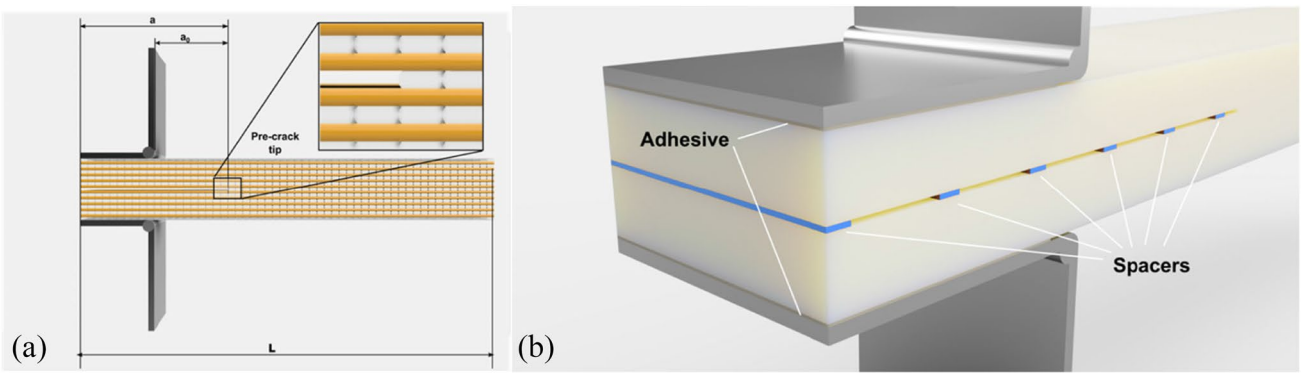

Fig. 2 (**a**) Schematic of the specimen adopted of DCB tests and (**b**) schematic of the sample prior of cutting the spacers used to produce the pre-crack

Table 3 Test matrix with factors and assumed levels

Level	Deposition strategy	Extrusion multiplier (%)	Deposition speed (mm/min)
I	±45°	96	1000
II	0/90°	100	2000
III		104	4000

2. Extrusion multiplier: Governing the volume of plastic extruded per unit distance through the print head's nozzle, this parameter was studied at three values: 0.96 (96%), 1.00 (100%), and 1.04 (104%).

3. Deposition speed: In this study, three different levels were considered: 1000, 2000, and 4000 mm/min for all deposition strategies. The printer used to produce the specimens is characterized by a maximum deposition speed of 9000 mm/min. However, such speed depends on several factors including the material characteristics as well as the layer height that influences the material flow. Preliminary tests were conducted to verify the suitability of the adopted speed levels to avoid possible errors or even danger to the machine.

For each test condition, four samples were manufactured, resulting in a total of 72 printed specimens.

2.4 Set up of the specimens and mechanical test

The load is transmitted to the specimen through the top and bottom layer surface. In fact, the load line must be perpendicular to these surfaces, promoting the transverse opening of the crack. To ensure this load condition, two steel piano hinges have been applied to the specimen, following the protocol below:

1. Apply a neutralizing cleaning spray (WEICON cleaner) to improve the quality of the adhesion between the specimen surface and the hinges. This product is necessary to remove all the contaminant elements, like the powder on both the surfaces of the specimen and the hinges.
2. White paint was applied to the specimen's side surface. Tick marks were marked every 5 mm each of them, starting from the crack tip (signed with 0) to determine the position of the crack front during the test were signed on this surface. In the first 5 mm starting from the sign 0, the marks were drawn 1 mm apart. This is crucial in the first part of the test as it will be explained in detail afterwards.
3. Subsequently, on the specimen's surfaces, at the hinge application area, is applied the Primer WEICON P400 chloric to prepare these surfaces before the application of the glue.
4. A two-component toughened methacrylate adhesive system AralditeÆ 2022–1 was applied to both the surfaces in the hinge area through a constant dosage pistol with a mixing nozzle. This area is limited by the width of the specimens and a distance from the specimen's border (where the crack starts) of 30 mm. This adhesive is supplied by Huntsman Corporation (TX, USA).
5. To provide a correct adhesion between the hinges and the specimen, it was necessary to wait at least 24 h after the bonding at normal ambient condition of temperature as stated in the DIN EN 1465 standard.

The entire process of specimen preparation was carried out with special care and attention, avoiding any possible damage to the specimens. In addition, during the mechanical tests, no fracture occurred between the hinge and the specimen.

The mechanical testing was executed using an MTS Universal Testing Machine, model C43.50, equipped with a 50 kN applied force capacity. For all the samples produced, great care during the first phase conforming to the requirements of the ASTM D5528 standards was taken. During this phase, the crack propagation was controlled by imposing a very slow traverse speed (1 mm/min), which aligns with the lowest velocity recommended by the corresponding standard. This enabled to keep low the bias introduced in this phase while being within the limits prescribed by the test standard.

To monitor the fracture tip, a Dino-Lite AM2111 traveling optical microscope with × 200 magnification, mounted on a movable base mechanism, was employed. The configuration of the test specimen on the machine is illustrated in Fig. 3.

The prescribed standard recommends splitting this mechanical test into two distinct phases. Specifically, the test was halted when the crack opening development, as recorded by the optical microscope, reached a value between 3 and 5 mm (Fig. 4). As mentioned in the second step of the specimen setup, the distance between two consecutive marks in the initial 5 mm from the crack tip is 1 mm. Consequently, the specimen was completely unloaded at a crosshead speed of 8 mm/min.

The objective of the first phase is to initiate the crack front and precisely determine the crack position. Additionally, it facilitates the elimination of any potential geometric imperfections introduced by the MEX process.

In the second phase, the test was resumed at a constant crosshead displacement speed of 1 mm/min. Throughout this stage, the load applied by the machine on the specimen was recorded alongside the corresponding value of the crosshead displacement and the crack tip position.

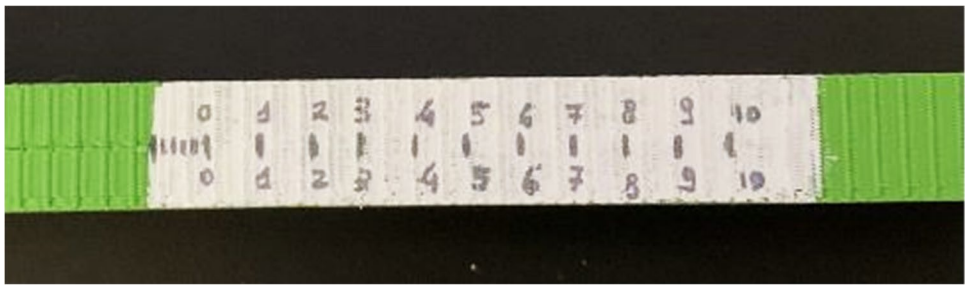

Fig. 3 Macrograph of the painted specimen adopted for the analysis of crack front propagation

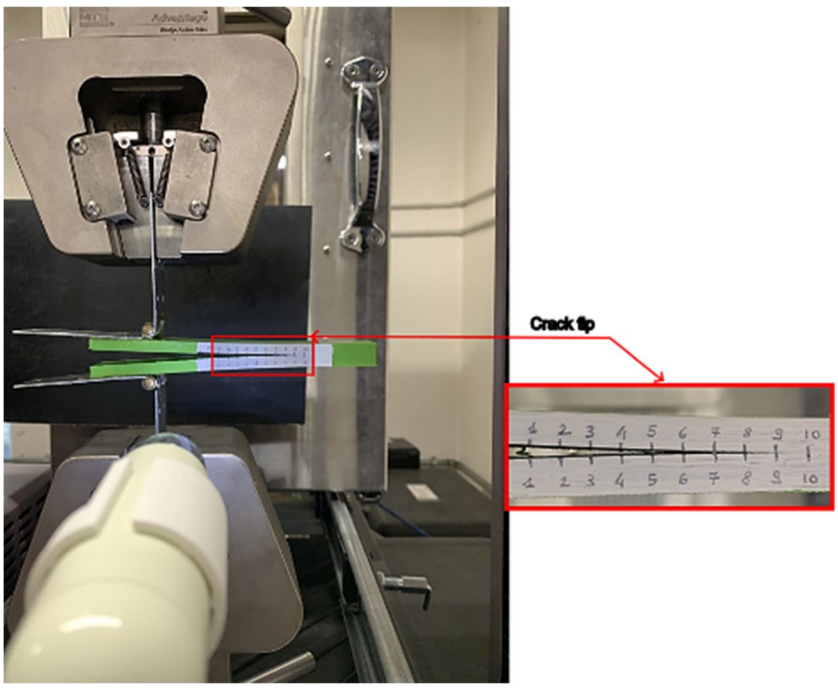

Fig. 4 Picture of the sample during the DCB test with a magnification of the measurement of the crack propagation

These three values were logged each time a crack front progression of 5 mm was observed through the optical microscope.

The critical energy release rate was determined using the VIS point technique. This method relies on visually identifying the initial crack motion through the microscope. Figure 5a illustrates two typical load-crosshead displacement diagrams for the two deposition strategies. The transparent plot represents the first part of the test, while the sharper one corresponds to the crack propagation resulting from the movement of the mobile crosshead displacement. All the point-markers depicted on the propagation diagram signify a 5 mm increase in the crack length.

The parameter Δ, depicted in Fig. 5b, represents the intercept of the linear regression curve between the cube root of C and the crack length that is the factor for calculating the critical energy release rate.

2.5 Characterization of the specimens

Thermo-gravimetric analysis (Mettler Toledo mod TGA/DSC3+, Milan, Italy) revealed the presence of $1.8 \pm 0.1\%$ residues probably due to the pigments. Calorimetric analyses were conducted by differential scanning calorimetry (Chip-DSC 100, Linseis Inc., Robbinsville, NJ, USA) with 10 °C/min heating/cooling rate. First heating was conducted from 25 to 190 °C; after 5-min annealing, cooling from 190 °C down to 25 °C was performed; after that, the specimen was heated again. Attenuated total reflectance/Fourier transform infrared (ATR-FTIR, Spectrum 100, Perkin-Elmer, Holding Ltd., London, UK) spectroscopy was conducted on the produced parts in the range 4000–650 cm^{-1}, with 4 cm^{-1} resolution. Scanning electron microscope (Phenom ProX, Phenom-World BV, Eindhoven, Netherlands) was adopted for characterizing the part surface after delamination. Before the analysis, parts were coated with thin gold film by sputtering. Dynamic mechanical

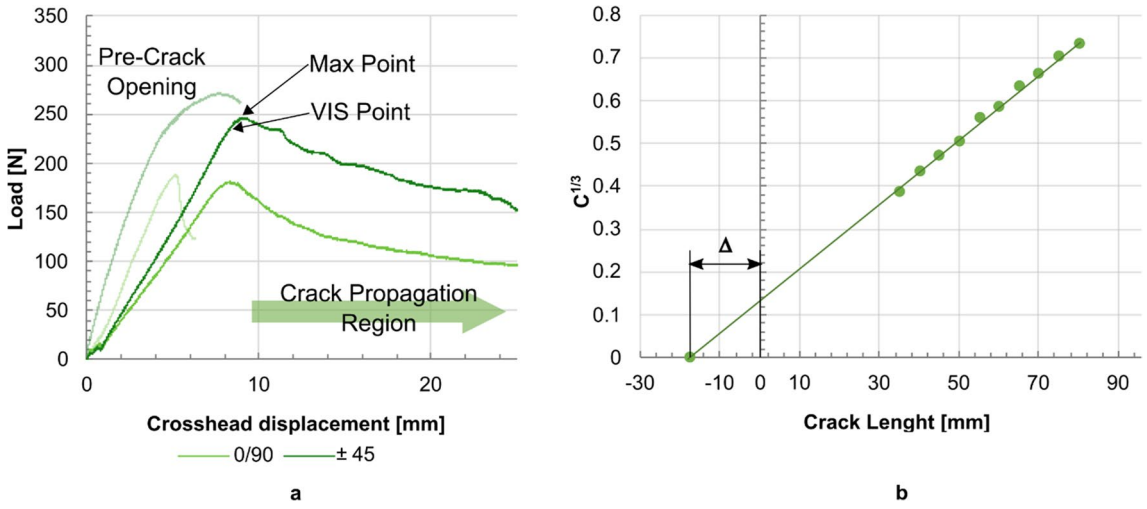

Fig. 5 Identification of the change in compliance starting from the load-crosshead displacement curve (**a**) and definition of the Δ factor for calculating the critical energy release rate (**b**)

analysis (DMA) was performed by Perkin-Elmer DMA8000 (Waltham, MA, USA) in tension mode, with 30 Hz, in the temperature range 25–105 °C, with 2 °C/min heating rate, and 50-µm displacement.

2.6 Temperature measurements

Thermal analysis was conducted using the infrared (IR) camera model E60 By Flir to investigate differences between samples produced with extrusion multipliers set at 100% and 104%, employing a constant printing speed (v) of 1000 mm/min. The IR camera was strategically positioned along the elongated side of the sample, capturing the entire deposition process. Securely fixed to the frame of the 3D printer, the camera maintained its position as the hot-end moved horizontally, while the sample progressed vertically, offering a comprehensive view of the deposition process. The emissivity calibration was performed through a comparative approach. Indeed, some thin samples (0.4 × 30 × 30 mm) were printed over the building plate. After printing, the temperature of the build plate was set to 60 °C, 80 °C, and 100 °C. For each condition, before proceeding with the temperature measurement, 120 s were lapsed with the aim of reaching steady-state conditions. Thus, the emissivity values were set so the temperature of the sample equals that of the plate (which was also measured through a K-type thermocouple). This enabled to establish a material emissivity of 0.87, irrespective of the build plate temperature.

3 Results

3.1 DCB tests and interlayer adhesion

Figure 6 shows the load-crosshead displacement curves obtained from the mode I tests conducted on samples produced under different processing conditions. The curves demonstrate two distinct behaviors primarily distinguished by the presence or absence of the crack propagation path. Only certain samples created with the 0/90° strategy lacked propagation, indicating poor interlayer adhesion and fracture toughness. Consequently, these samples exhibited a null fracture toughness as the crack immediately propagated during the preliminary phase of the tests. Specifically, all samples created with the extrusion multiplier set to 104% showed the crack propagation path, irrespective of the deposition speed used. In contrast, under the lower extrusion multiplier conditions (i.e., $EM = 96\%$ and $EM = 100\%$), the sole deposition speed that led to crack propagation was 2000 mm/min, while under the other conditions (1000 mm/min and 4000 mm/min), a brittle fracture behavior was observed.

Conversely, all samples produced with the ± 45° strategy exhibited a crack propagation path, highlighting the significant sensitivity of fracture toughness to the loading path, as depicted in Fig. 7. Notably, the 0/90° samples

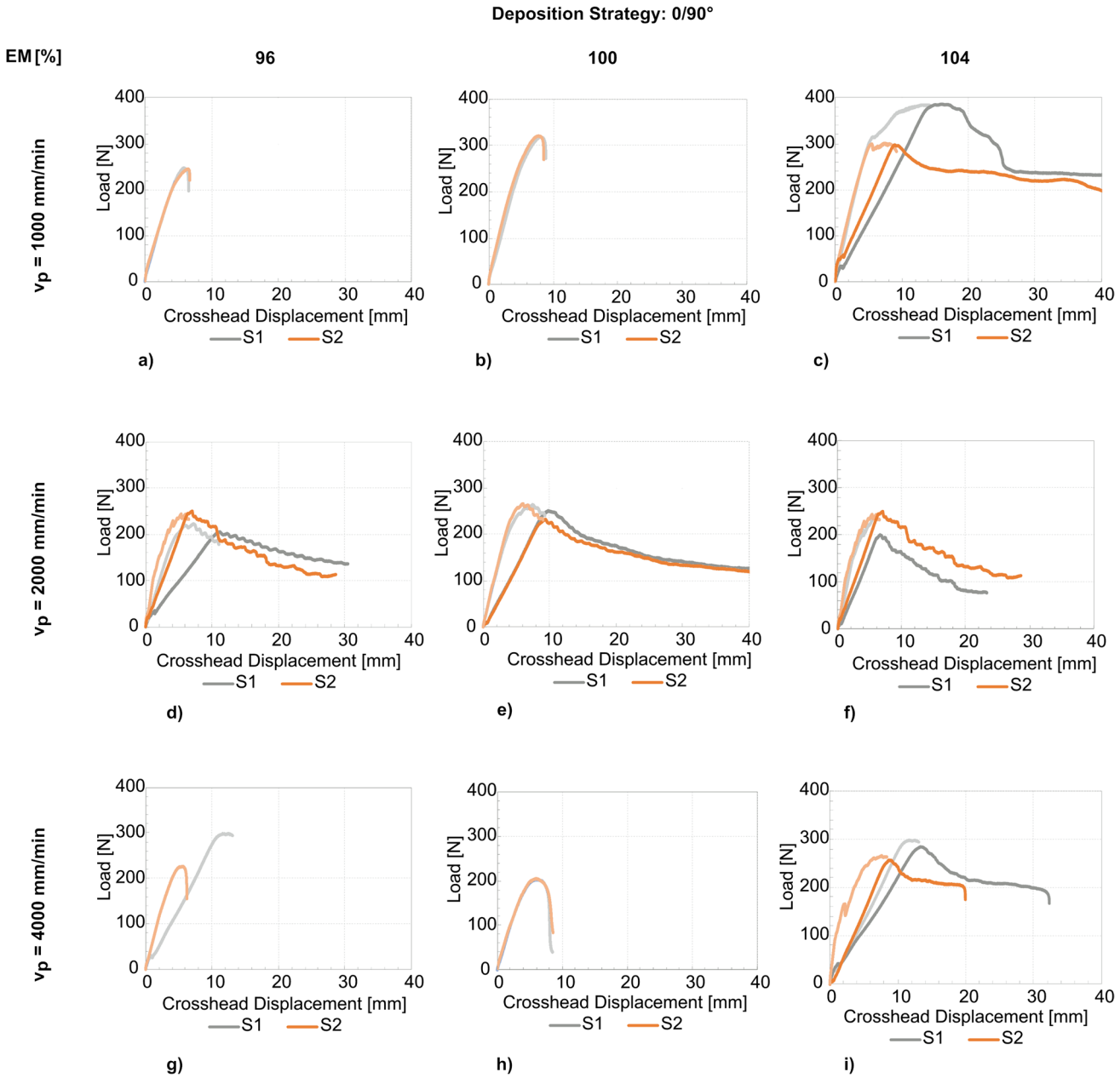

Fig. 6 Load-crosshead displacement charts obtained from the 0–90 specimens tested related to the test matrix, with several extrusion multipliers (EM). The transparent curves represent the initial crack opening, while the sharper curves correspond to the stable propagation phase. For each testing condition, just two curves S1 and S2 were reported

revealed a substantial increase in fracture toughness with an increase in the extrusion multiplier from 96 to 104%. Additionally, the deposition speed significantly influenced the crack propagation behavior. Specifically, for $EM = 96\%$ and $EM = 100\%$, the adoption of the lowest (1000 mm/min) and the highest (4000 mm/min) deposition speeds resulted in no fracture propagation. However, under the intermediate deposition speed (2000 mm/min), the crack propagation path was observed, regardless of the extrusion multiplier used.

In the load-crosshead displacement curves of samples manufactured using the 0/90° strategy with a deposition speed of 2000 mm/min, an intriguing observation surfaced. Particularly, when the extrusion multipliers were set to lower values ($EM = 96\%$ and $EM = 100\%$), the crack propagation path exhibited a distinct stepped decay pattern, depicted in the magnified illustration. This abrupt drop tended to diminish in samples printed with an EM of 104%, where the crack propagation displayed a smoother, more continuous decline. This behavior was attributed to the structural characteristics

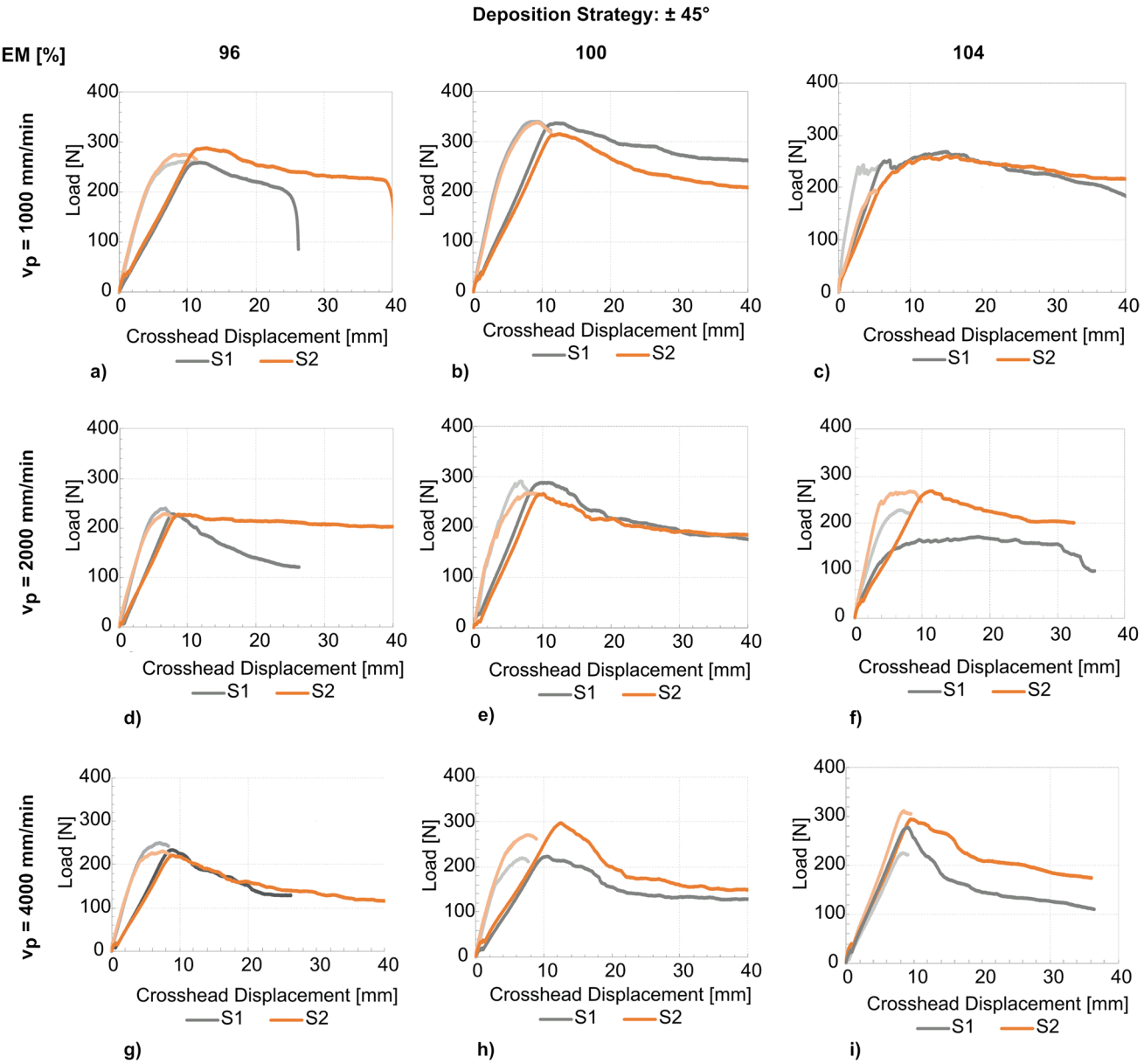

Fig. 7 Load-crosshead displacement charts obtained from the ± 45° specimens tested related to the test matrix. The transparent curves represent the initial crack opening, while the sharper curves correspond to the stable propagation phase

of the samples and the filament arrangement concerning the loading path. Samples created with lower extrusion multipliers demonstrated wider gaps between consecutive filaments, leading to a load drop as the crack traversed a filament perpendicular to the load (90° filaments), as can be noted in Fig. 8. Conversely, an increase in the extrusion multiplier resulted in narrower gaps between filaments, fostering a more consistent load decay.

Conversely, in the samples produced with the ± 45° strategy, the stepped pattern was consistently absent. Regardless of the deposition conditions, the crack opening exhibited a continuous decay in load. Indeed, in samples created with the ± 45° strategy, no filament was perpendicular to the crack propagation direction, enabling a more uniform load distribution along the filaments and preventing the stepped decay observed in the 0/90° samples.

Based on the analysis of force–displacement curves and observations of crack propagation, the computation of the energy release rate was conducted utilizing the modified beam theory equation (Eq. 8), following the methodology outlined in Sect. 3. Figures 6 and 7 were generated based on the approach illustrated in Fig. 5. It is crucial to emphasize that all specimens that completed both stages of the test showcased two distinct curves: the transparent curves

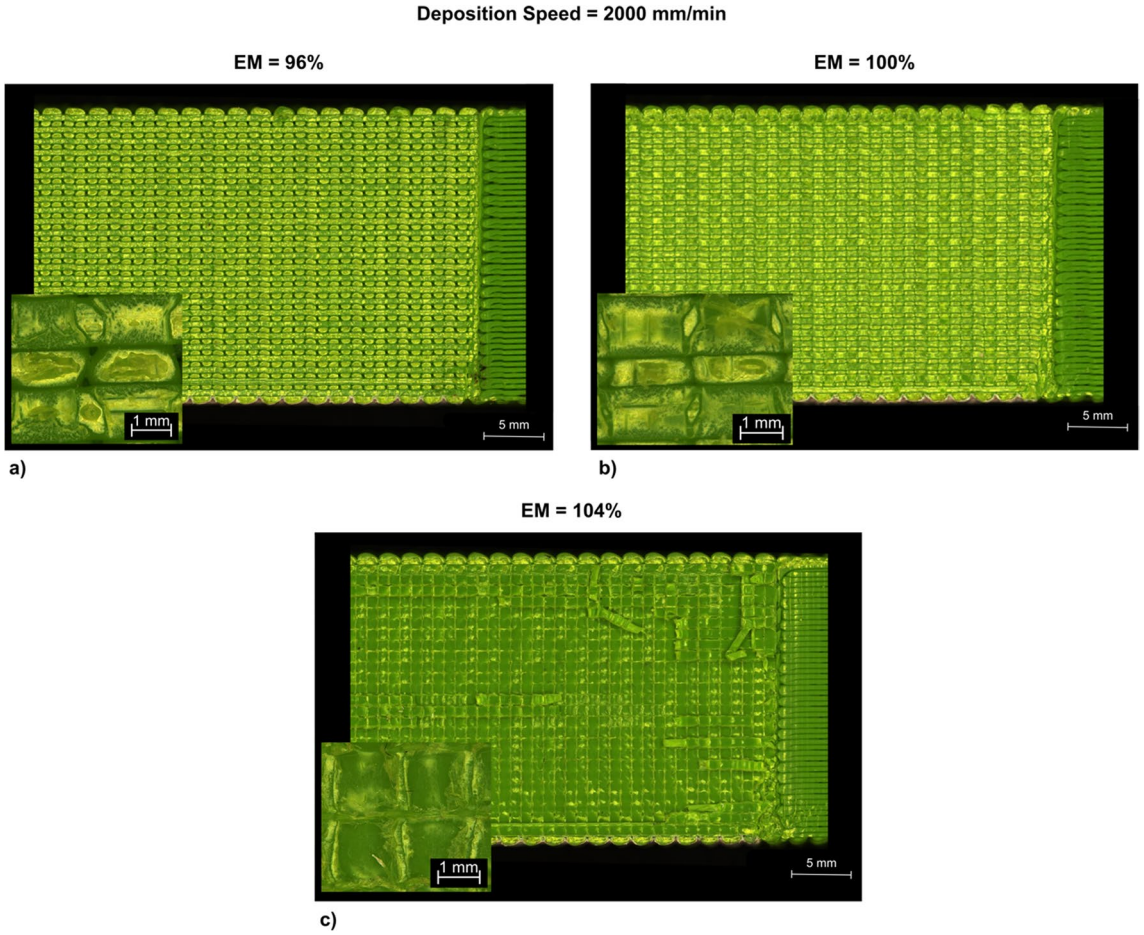

Fig. 8 Fracture surface of specimens produced with varying the extrusion multiplier **a** $EM = 96\%$, **b** $EM = 100\%$, and **c** $EM = 104\%$

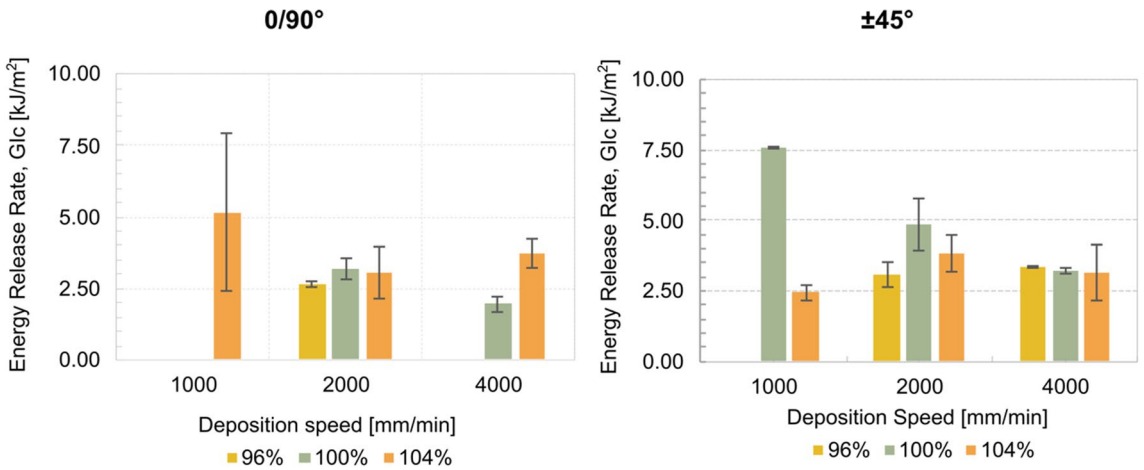

Fig. 9 Influence of the process parameters (extrusion multiplier and deposition speed) on GIc using different deposition strategies: **a** 0/90° and **b** ±45°

represent the initial crack opening, while the sharper curves correspond to the stable propagation phase. Notably, the 0/90° specimens exhibited brittle behavior during the initial crack propagation in multiple samples, with some displaying out-of-plane crack propagation relative to the nominal direction introduced during the MEX process. Consequently, this led to the inability to compute GIc and subsequent test failure in certain cases, as depicted in Fig. 9. In contrast, the ± 45° deposition strategy induced increased plasticity during the initial crack displacement, likely owing to the path orientation between consecutive layers. Another key difference between the two specimen types is apparent in the crack propagation region depicted on the load-crosshead displacement charts in Figs. 6 and 7. As reported in [16], the ± 45° samples exhibited a consistent release of fracture energy during the propagation phase, while the 0/90° samples showed load drops associated with crack propagation through consecutive filaments.

The results reported in Fig. 9 are also summarized in Table 4.

3.2 Fracture surface analysis by optical microscopy

Contrary to initial expectations, the increase in the extrusion multiplier did not yield a consistent rise in fracture toughness. The higher flow rate of extruded material was anticipated to enhance pressure and heat transfer on the underlying layers, thereby fostering improved interface adhesion. This was attributed to the more effective rearrangement of polymer chains between overlapping filaments in two consecutive layers. Notably, the investigation of the four deposition conditions was extended through microscopic analysis utilizing a LEICA M205A stereoscope, as depicted in Fig. 10.

Surprisingly, specimens produced with an extrusion multiplier of 104% displayed weak adhesion, as clearly discernible in Fig. 10b and d. These images illustrate extensive areas where the initial crack propagates with a simple detachment between the two overlapping layers. Notably, the magnified images of the repetitive unit cell (RUC) indicate that the filaments deposited between successive layers remained largely intact, with only sporadic regions offering higher resistance to crack progression. These areas are distinguished by brighter regions compared to the original filament color, albeit visible only partially in the RUCs and the entire adhesion region in these two images. Conversely, the images in Fig. 10a and c demonstrate that the filaments of one layer were dragged by the overlying layer. These images reveal substantial damage not only at the interface but also internally within the single layer; this confirms the higher load-bearing capacity of these samples. In both the RUC and the overall view, these images appear notably brighter than those in Fig. 10b and d, likely owing to the superior resistance to defect propagation exhibited by components with an extrusion multiplier of 100%.

Table 4 Experimental results from mode I tests

Deposition strategy	Printing speed (mm/min)	*EM* (%)	Average GIc (kJ/m^2)	σ GIc (kJ/m^2)
	1000	96	0	0
		100	0	0
		104	5.16	2.74
0/90	2000	96	2.66	0.07
		100	3.19	0.36
		104	3.04	0.91
	4000	96	0	0
		100	3.22	0.08
		104	3.73	0.51
	1000	96	0	0
		100	7.58	0.04
		104	2.44	0.25
± 45°	2000	96	3.10	0.45
		100	4.85	0.94
		104	3.85	0.65
	4000	96	3.36	0.05
		100	3.22	0.08
		104	3.16	0.96

3.3 Thermal analysis

The infrared image acquired during printing is depicted in Fig. 11a, revealing distinct regions such as the hot-end, extruded material, and the sample.

To discern and quantify temperature variations between samples produced under different processing conditions, a measurement point was designated on the upper surface of the sample. Figure 11b compares the thermal histories recorded during two depositions at a constant speed of 1000 mm/min and an extrusion angle of ± 45°. Temperature trends displayed peaks of approximately 210 °C as the hot-end traversed the measurement point, followed by a rapid decrease. Notably, these temperature peaks were consistent for both *EM* = 100% and *EM* = 104%. However, a significant discrepancy was observed in the substrate temperature. For *EM* = 100%, the mean substrate (underlying layer) temperature was approximately 59 °C, while for *EM* = 104%, it rose to almost 70 °C.

A detailed examination of the temperature history during layer deposition is presented in Fig. 11c. It is evident that the use of a higher extrusion multiplier (*EM* = 104%) resulted in a slower cooling rate and higher average temperature compared to the adoption of a lower extrusion multiplier (*EM* = 100%). This behavior can be attributed to the increased flow rate with higher *EM* values,

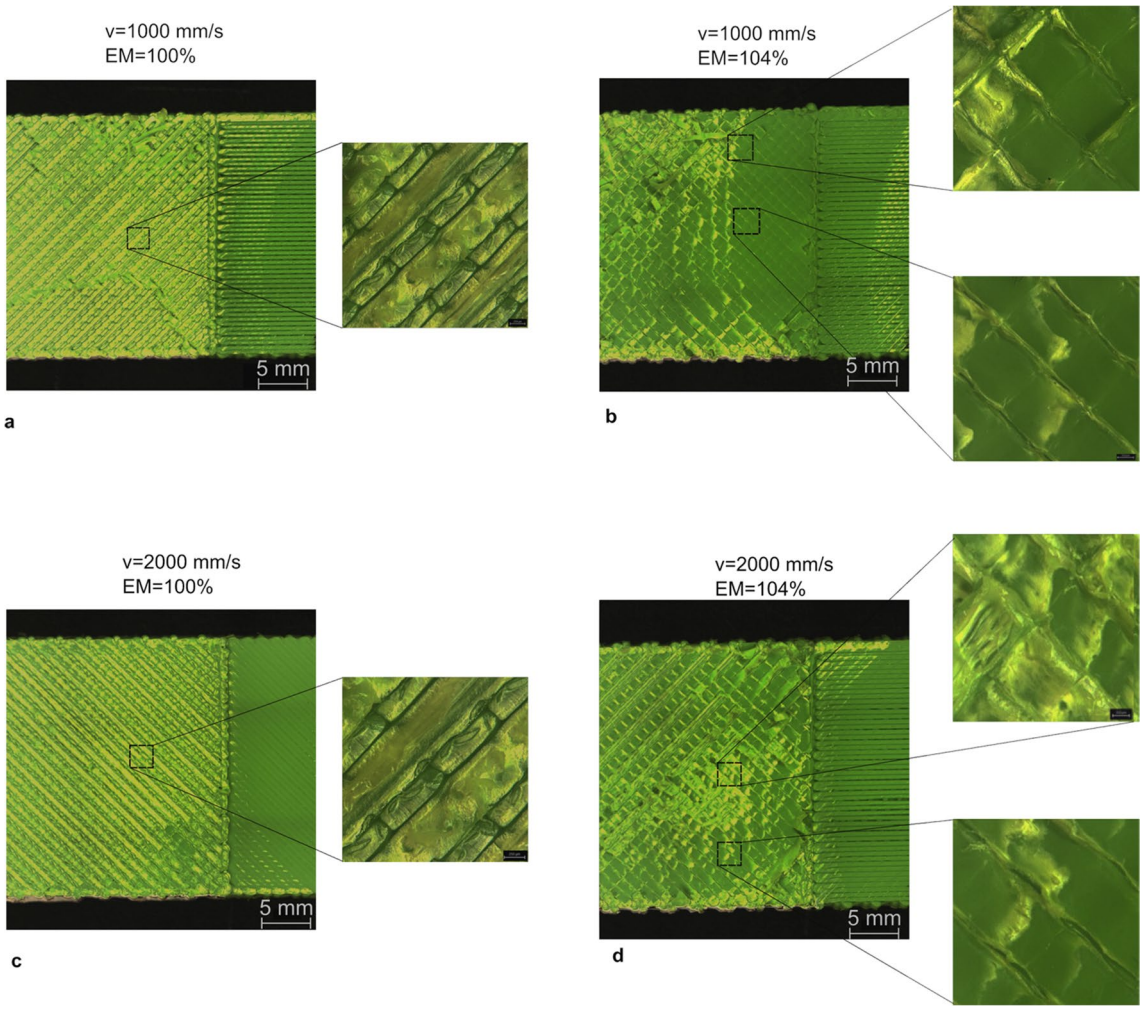

Fig. 10 Fracture surface observed through optical microscopy of samples made under reference deposition conditions: **a** $v = 1000$ mm/min, $EM = 100\%$; **b** $v = 1000$ mm/min, $EM = 104\%$; **c** $v = 2000$ mm/min, $EM = 100\%$; **d** $v = 2000$ mm/min, $EM = 104\%$

consequently augmenting thermal inertia and leading to reduced cooling rates and elevated average temperatures, in contrast to the conditions observed with $EM = 100\%$. However, it has to be pointed out that an increase in *EM* may lead to an incomplete melting.

3.4 DMA and DSC analysis

These samples were subsequently further analyzed through additional techniques. Figure 12 shows the DMA analyses conducted on the specimens obtained with different *EMs*, 100 and 104, in terms of storage modulus and tan d, which represents the ratio between loss and storage modulus.

The specimen obtained with $EM = 100\%$ shows a slightly lower storage modulus (at the lower temperatures) and a higher glass transition temperature (see also the maximum value of tan d) than the specimen obtained with $EM = 104\%$. The storage modulus decreases when the temperature reaches the values of the glass transition; however, after the minimum, it increases again, due to the incoming crystallization. The specimen obtained with $EM = 100\%$ shows a higher storage modulus increase; this may be due to a smaller crystallinity degree achieved during the deposition process. Conversely, the specimen obtained with $EM = 104\%$ shows a smaller increase in the storage modulus after the minimum value, suggesting a higher crystallinity degree achieved during the deposition process. The higher values of the crystalline degree of the specimen obtained with $EM = 104\%$ could be due to both slower cooling rate during deposition (see Fig. 10c) and the presence of nuclei due to incomplete melting. Figure 13a, related to the calorimetric analyses of the 3D printed parts, confirms this assumption.

The calorimetric analysis conducted on the filament revealed a high crystalline degree. The calorimetric analyses

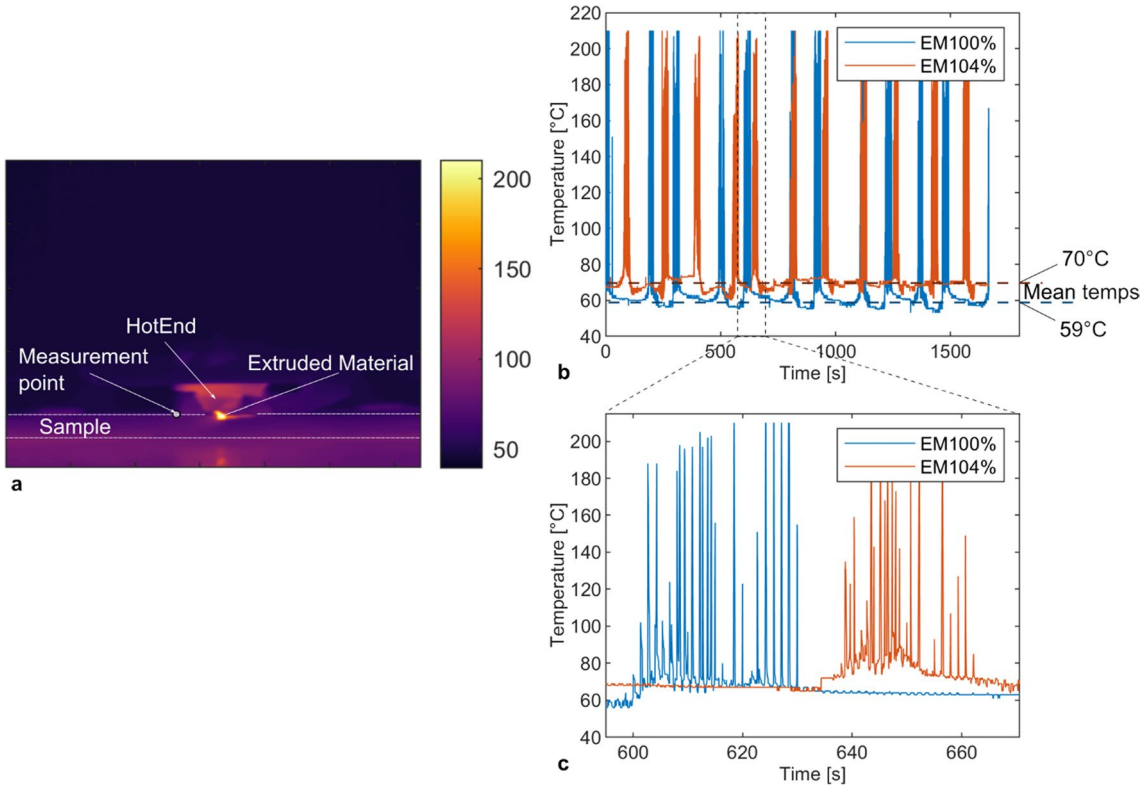

Fig. 11 **a** IR temperature maps acquired during the deposition of the samples, **b** temperature history at the measurement point (on the top surface of the sample) under different deposition conditions, and **c** temperature history during the deposition of a single layer

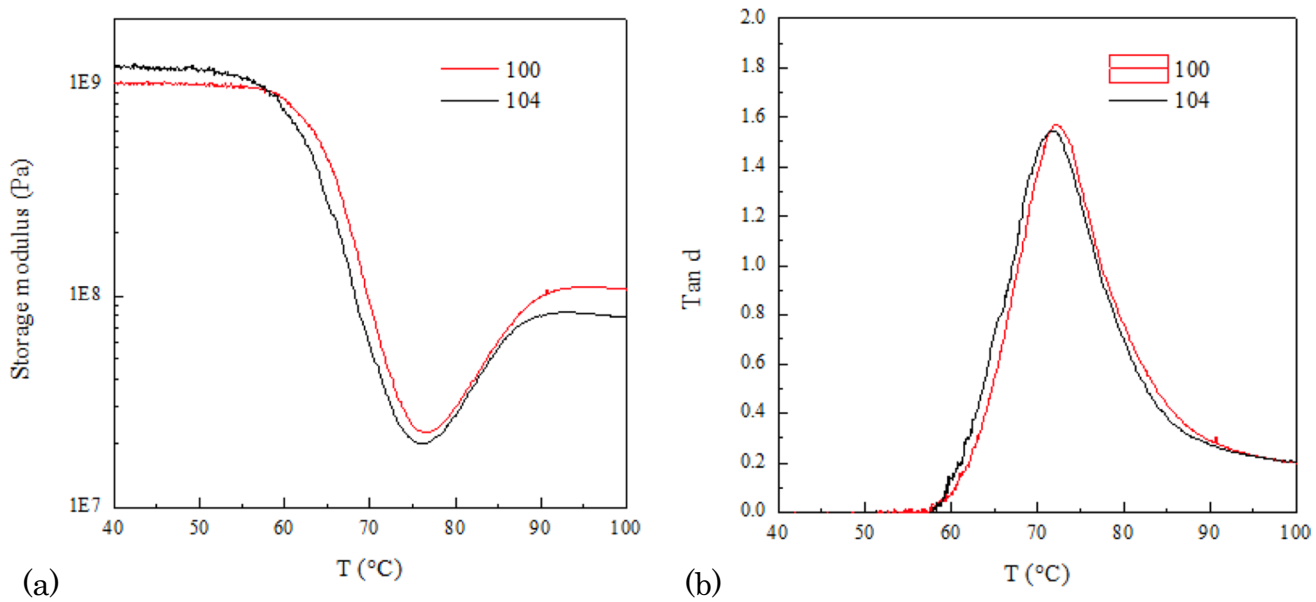

Fig. 12 DMA analysis conducted on the specimens obtained with different EMs. **a** Storage moduli and **b** tan d

on 3D printed parts show, for both *EMs*, exothermic peaks ascribable to the cold crystallization arising during the analysis. Such an exothermic peak confirms that the fast cooling occurring during the process leads to the formation of mostly amorphous parts. Interestingly, the endothermic peak due to the melting moves toward lower temperatures for the parts

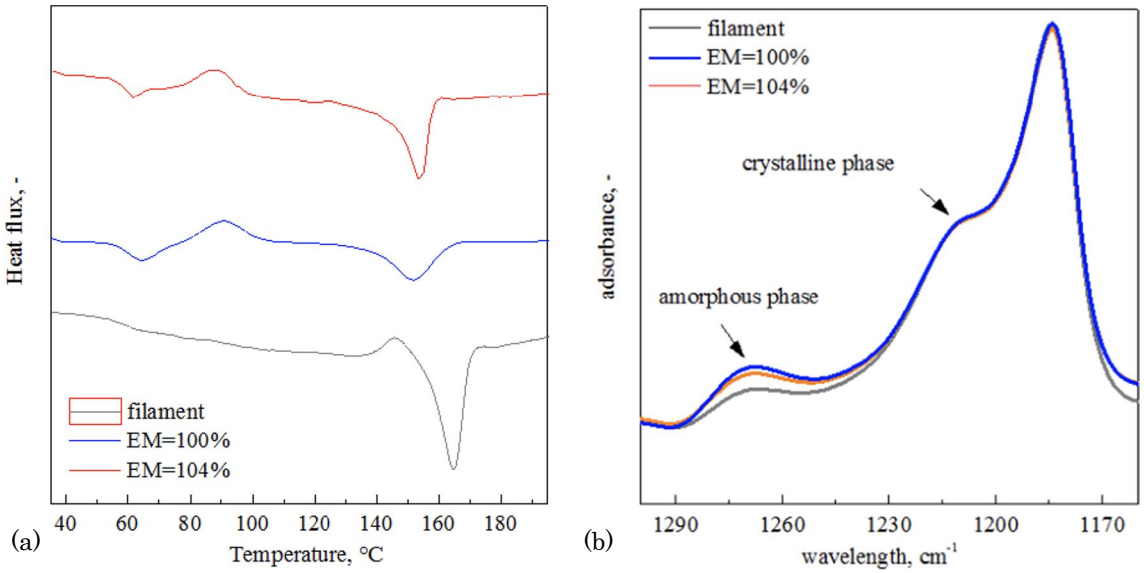

Fig. 13 **a** DSC analyses and **b** ATR spectra for the specimens obtained with different EMs. The analyses of the filament are also reported for comparison

produced by MEX. This could be ascribed to the formation of a different crystalline phase during the process [30]. DSC analyses essentially confirm what has been found by DMA analyses: the part obtained with $EM = 104\%$ shows a higher crystalline degree than the part obtained with $EM = 100\%$. Figure 13b shows the ATR spectra of 3D printed parts and the filament in the range 1300–1160 cm^{-1}. Two characteristic peaks can be detected: at 1210 cm^{-1}, related to C–O–C stretching vibration of the carbonyl group, characteristic of the crystalline phase, and 1270 cm^{-1}, characteristic of the amorphous phase [31]. 3D printed parts show higher intensity of the peak characteristic of the amorphous phase, consistently with those already observed from DSC analyses. Parts obtained with $EM = 100\%$ show a higher amount of amorphous phase than the parts obtained with $EM = 104\%$. It must be noticed that ATR reveals information about the external part of the deposited layer, whereas DSC analysis is averaged on the whole specimen. Even if related to different areas of the deposited layer, the analyses are consistent and confirm that $EM = 104\%$ leads to slightly higher crystallinity.

SEM analyses allow us to investigate structures present in the part at the delamination (see Fig. 14).

SEM micrographs clearly reveal that delamination induces the detachment of adjacent layers and that the extension of the detached area depends on the extrusion multiplier: for $EM = 100\%$, a larger detached area was observed. Furthermore, the detached area of the part obtained with $EM = 104\%$ was smoother than the one observed for the part obtained with $EM = 100\%$ (compare Fig. 14a and b); this is a clear indication that the increase of EM to 104% led to weaker adhesion. Figure 14d shows the presence of ordered structures, probably due to the presence of spherulites, on the surface of the deposited layers, such a finding is consistent with a higher crystallinity degree for the part obtained with $EM = 104\%$.

Crossing the information provided by different analyses, it was hypnotized that for the part obtained with $EM = 104\%$, the crystallization must occur before the polymer chain could diffuse at the interface between adjacent layers, hindering any additional diffusion. In the case of the part obtained with $EM = 100\%$, crystallization was slow enough to allow a significant polymer chain diffusion at the interface, leading to a stronger adhesion. The higher crystallinity degree of the parts obtained with $EM = 104\%$ can be ascribed to the presence of small crystals already at the exit of the liquefier which makes the crystallization process faster, limiting, therefore, the rearrangement of polymer chains at the interface.

4 Discussion

The investigation into the impact of deposition strategy, encompassing material flow and travel speed, on interlayer adhesion in the material extrusion (MEX) process has yielded significant insights. The MEX process, while celebrated for its efficiency and versatility, hinges on the cohesive strength of interlayer bonds to ensure mechanical integrity. The experimental tests from the study, employing mode I fracture toughness as a pivotal parameter, shed light on the nuanced interplay between deposition parameters and the resultant interlayer adhesion.

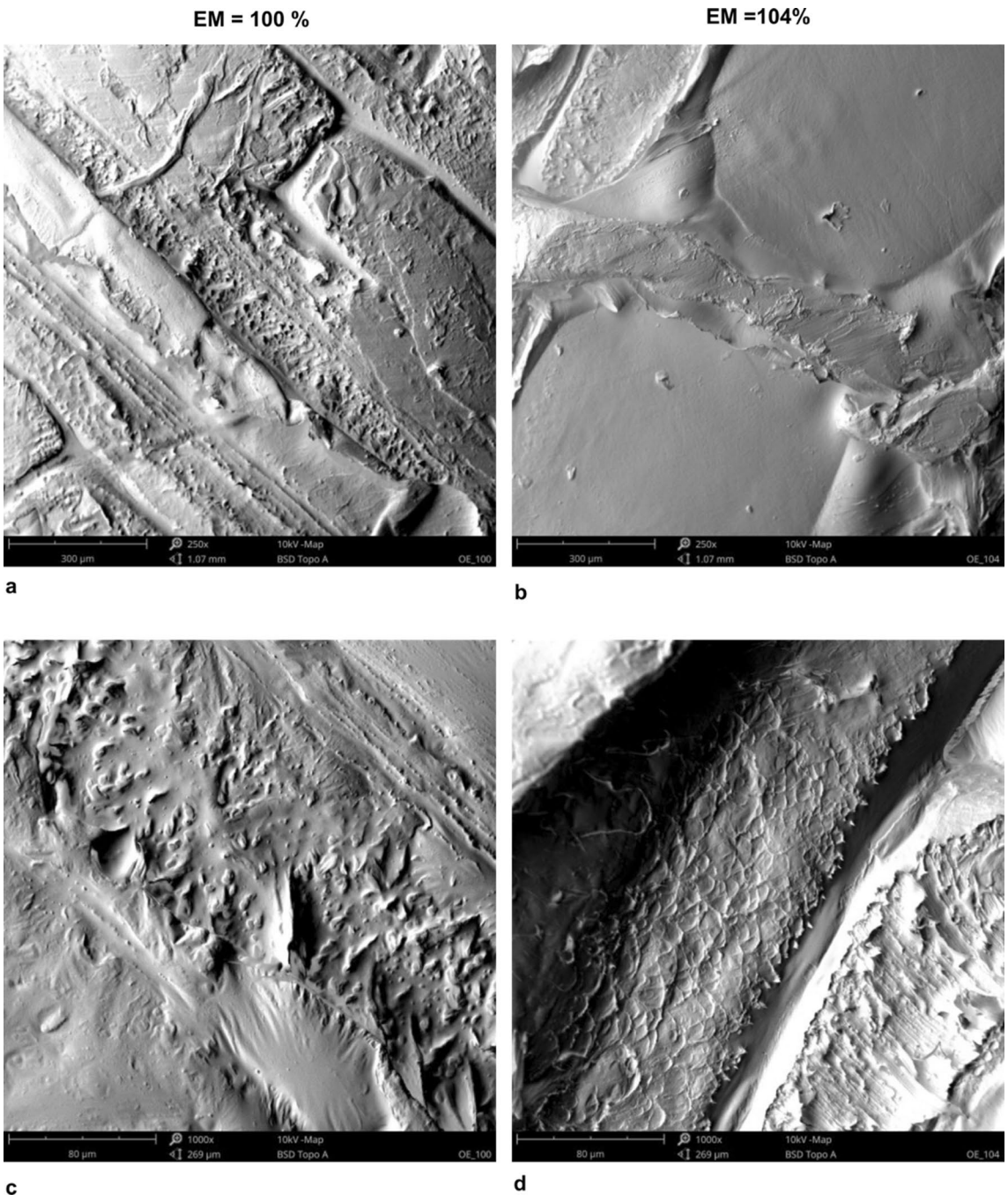

Fig. 14 SEM micrographs obtained with two magnifications, ×250 (**a**, **b**) and ×1000 (**c**, **d**), for the parts obtained with 100 and 104 *EM*, after the delamination test

The observed trend indicates a profound influence of material flow rate on interlayer adhesion. Optimal material flow facilitates consistent layer bonding, minimizing the potential for voids or irregularities. The obtained results revealed unanticipated trends. An increase in the extrusion multiplier, which correlates with a reduction in void dimensions, is anticipated to enhance deposition toughness. Conversely, the highest energy release rate was observed at a deposition speed of 1000 mm/min (the minimum deposition speed used) and 100% infill (representing the intermediate infill percentage). Under these conditions, with filaments oriented at ± 45°, the energy release rate GIc reached 7.5 kJ/m^2. However, the same deposition conditions resulted in significantly weaker deposition when the filaments were oriented at 0/90° relative to the sample direction.

A balanced approach, yielding a high energy release rate for both 0/90° and ± 45° loading directions, was achieved with a deposition speed of 2000 mm/min and an intermediate infill percentage of 100%. This finding suggests that the highest infill percentage does not necessarily provide the optimal solution. Fracture surface analysis indicated weaker interlayer adhesion with an extrusion multiplier set at 104% compared to 100%. Temperature analysis during the MEX process revealed significant differences in mean temperature associated with varying extrusion multipliers. Additionally, higher printing speeds and increased material flow (via higher extrusion multipliers) may result in incomplete filament melting. This incomplete melting can contribute to increased crystallization during deposition, originating from existing crystalline regions in the filament. Such crystallization is detrimental as it can impede molecular chain mobility, thereby reducing interlayer molecular chain entanglement.

The intricate link between travel speed and interlayer adhesion was elucidated. Slower deposition speeds exhibited a positive correlation with enhanced interlayer bonding, aligning with the fundamental principles of the material extrusion process. The travel speed influences the melting degree reached by the polymer inside the extruder through the residence time. The higher the travel speed, the shorter the residence time is. This leads to an incomplete melting that induces faster solidification [28]. Cakmak et al. [29] demonstrated that polymer chains have to experience high temperatures (above the melting temperature) for time sufficiently long to allow complete melting. In the case of semicrystalline polymers, the presence of crystalline nuclei would yield a "self-seeding" effect that would enhance the crystallization kinetics during deposition.

On the other hand, higher travel speeds led to diminished interlayer adhesion, emphasizing the significance of finding an equilibrium between efficiency and structural integrity.

The material flow, which was varied through the extrusion multiplier, also showed a strong influence on the interlayer adhesion. This effect was more pronounced in sample printed at lower deposition speeds. Under such conditions, the adoption of higher extrusion multiplier yielded to weaker interlayer adhesion even though it yielded higher mean temperatures of the substrate. This effect was addressed to two phenomena: incomplete melting of the crystalline phase within the filament and the possible development of crystalline phase during the deposition owing to different cooling rates.

Identifying these dependencies underscores the critical importance of optimizing deposition strategies. Neglecting this equilibrium could result in compromised mechanical properties and structural reliability, impacting various industries reliant on additive manufacturing. By fine-tuning deposition strategies, manufacturers can enhance product quality, reduce failure risks, and foster the adoption of additive manufacturing for critical applications.

Even though the adoption of IR thermography enabled to determine the temperature gradients and variation during the deposition, this technique involved a technical difficulty to determine the cooling rates at the layer interface. Indeed, these are the regions that primarily influence the interlayer adhesion. In addition, even though the DSC enabled to identify crystalline regions, this analysis tended to average (through the melting enthalpy) the crystalline percentage between the layer core (where slower cooling rates take place) and that developed at the layer surface.

This research contributes to establishing foundational principles for achieving superior interlayer bonding, ultimately advancing the reliability and applicability of MEX-produced components. Further research avenues may involve exploring additional fracture toughness modes and integrating advanced computational simulations to deepen our understanding of interlayer adhesion mechanisms in additive manufacturing. At the light of the above-mentioned limitations, extensive characterization campaigns are still required, given a specific material, to determine the optimal deposition conditions that allow to maximize the interlayer adhesion. This indicates that more efforts are still required to set up an experimental procedure (maybe integrated with numerical models of the thermal history during the deposition) that enables to predict with high accuracy of the interlayer adhesion properties based on the selected deposition conditions. In addition, the results pointed out the great relevancy of the unmolten crystalline phase after the extrusion that depends on the material flow and that may hinder the interlayer adhesion. Thus, further studies should be conducted to determine how the material flow and temperature of the extruder influence the percentage of the unmolten material and consequently the crystalline phase.

5 Conclusions

This study focused on investigating the interplay between deposition strategy, including material flow and travel speed, and its impact on interlayer adhesion. Through experimental tests utilizing mode I fracture toughness tests, insights were gained into the critical relationship between deposition parameters and the resulting adhesion strength. The findings underscore the significance of meticulous parameter control to achieve optimal interlayer bonding. This understanding contributes to advancing the efficacy and reliability of additive manufacturing processes, fostering enhanced component integrity in various applications. The main results from the study are summarized as follows:

- The alternate deposition strategy of ± 45 resulted to be more reliable than the 0/90. In average, the values of the fracture toughness are higher for all the different analyzed cases.
- The 0/90 deposition strategy requires the highest values of the extrusion multiplier (104%) to obtain a compliant interlayer bonding. In any case, an improvement of the fracture toughness was monotonically observed with the diminishing of the printing speed. For a value of the $EM = 104\%$, the maximum value of the obtained GIc was equal to 5.16 kJ/m^2, obtained with a feed rate of 1000 mm/min.
- Reducing the printing speed had a positive impact on the bonding between consecutive layers. Indeed, for a value of the $EM = 96\%$, only specimens printed at the flow rate of 2000 mm/min were allowed to obtain results from the mode I tests in the case of the 0/90 deposition strategy. The obtained average value for the fracture toughness is 5.2 kJ/m^2.
- Specimens printed with a ± 45 layers' orientation showed the highest GIc for an *EM* of 100%. In this case too, the highest average value of the fracture toughness is 7.6 kJ/m^2, obtained at the printing speed of 1000 mm/min. The values of *EM* of 96% and 104% show similar results for this category of specimens, with average values approximately close to 3.5 kJ/m^2.
- The adoption of an extrusion multiplier $EM = 104\%$ led to weaker fracture toughness as compared to the samples printed with $EM = 100\%$. This was due to higher crystallinity observed in samples made with $EM = 104\%$ which significantly hindered molecular entanglement between layer interfaces.
- The adoption of filaments with crystalline phase may be detrimental especially when printing at high material flow rates (e.g., high printing speed and extrusion multipliers). Indeed, the incomplete melting of the filament and the presence of the crystalline phase during the material deposition may hinder the molecular chain mobility, and consequently, it may reduce the interlayer chain entanglement and interlayer adhesion.

Acknowledgements This research was conducted within the project "ARS01_00536 PON 2014-2020—OCEANOS—Crop and Coastal Marine Monitoring: New Generation Satellite Technologies" which was granted by the Italian Ministry of Education and Research.

Author contribution Francesco Lambiase: conceptualization, methodology, investigation, resources, data curation, writing—original draft, supervision, project administration. Sara Liparoti: conceptualization, methodology, investigation, resources, data curation, writing—original draft, supervision. Francesco Pace: conceptualization, investigation, data curation, writing—original draft. Silvia Ilaria Scipioni: investigation, data curation, writing manuscript. Alfonso Paoletti: conceptualization, resources, writing—original draft, supervision, project administration.

Funding Open access funding provided by Università degli Studi dell'Aquila within the CRUI-CARE Agreement.

Data availability Data will be made available on request.

Declarations

Competing interests The authors declare no competing interests.

References

1. Durão LFC, Christ A, Anderl R, Schützer K, Zancul E (2016) Distributed manufacturing of spare parts based on additive manufacturing: use cases and technical aspects. Procedia CIRP 57(704–709):2212–8271
2. Nazir A, Gokcekaya O, Billah KMM, Ertugrul O, Jiang J, Sun J, Hussain S (2023) Multi-material additive manufacturing: a systematic review of design, properties, applications, challenges, and 3D printing of materials and cellular metamaterials. Mater Des 111661:0264–1275
3. Cao D (2024) Increasing strength and ductility of extruded polylactic acid matrix composites using short polyester and continuous carbon fibers. J Adv Manuf Technol 130:3631–3647
4. Lambiase F, Scipioni SI, Paoletti A (2022) Determination of local density in components made by fused deposition modeling through indentation test. J Adv Manuf Technol 122:1467–1478. https://doi.org/10.1007/s00170-022-09986-4,0268-37681433-3015
5. Glinz J, Pace F, Maurer J, Holzleitner M, Eckl M, Vopálenský M, Kumpová I, Kastner J, Stamopoulos A, Senck S (2023) Influence of continuous fiber reinforcement on tensile properties in fused filament fabricated specimens, AIAA SCITECH 2023 Forum: 2199. https://doi.org/10.2514/6.2023-2199
6. Liu X, Shan Z, Liu J, Xia H, Ao X, Zou A, Wu S (2022) Mechanical and electrical properties of additive manufactured high-performance continuous glass fiber reinforced PEEK composites. Compos B Eng 247(110292):1359–8368
7. Abderrafai Y, Diouf-Lewis A, Sosa-Rey F, Farahani RD, Piccirelli N, Lévesque M, Therriault D (2023) Additive manufacturing and characterization of high temperature thermoplastic blends for potential aerospace applications. Compos Sci Technol 231(109839):0266–3538
8. Yi N, Davies R, Chaplin A, McCutchion P, Ghita O (2021) Slow and fast crystallising poly aryl ether ketones (PAEKs) in 3D printing: crystallisation kinetics, morphology, and mechanical properties. Addit Manuf 39(101843):2214–8604
9. Hamat S, Ishak M, Sapuan S, Yidris N, Hussin M, Abd Manan M (2022) Influence of filament fabrication parameter on tensile strength and filament size of 3D printing PLA-3D850. Mater Today: Proceedings 2214–7853

10. Lambiase F, Scipioni SI, Paoletti A (2023) Mechanical characterization of FDM parts through instrumented flat indentation. Int J Adv Manuf Technol 125:4201–4211. https://doi.org/10.1007/s00170-023-10992-3,0268-37681433-3015
11. Scipioni SI, Lambiase F (2023) Yielding and post-yielding behavior of FDM parts under compression stress, Int J Adv Manuf Technol 128:1199–1211. https://doi.org/10.1007/s00170-023-11985-y
12. Durão LFC, Barkoczy R, Zancul E, Lee Ho L, Bonnard R (2019) Optimizing additive manufacturing parameters for the fused deposition modeling technology using a design of experiments. Prog Addit Manuf 4(291–313):2363–9512
13. Durão LFCS, Barkoczy R, Zancul E, Lee Ho L, Bonnard R (2019) Optimizing additive manufacturing parameters for the fused deposition modeling technology using a design of experiments. Prog Addit Manuf 4:291–313. https://doi.org/10.1007/s40964-019-00075-9,2363-95122363-9520
14. Gao X, Qi S, Kuang X, Su Y, Li J, Wang D (2021) Fused filament fabrication of polymer materials: a review of interlayer bond. Addit Manuf 37(101658):2214–8604
15. Liparoti S, Sofia D, Romano A, Marra F, Pantani R (2021) Fused filament deposition of PLA: the role of interlayer adhesion in the mechanical performances. Polymers 13(3):399. https://doi.org/10.3390/polym13030399
16. Lambiase F, Stamopoulos AG, Pace F, Paoletti A (2023) Influence of the deposition pattern on the interlayer fracture toughness of FDM components, Int J Adv Manuf Technol 128:4269–4281
17. Spoerk M, Gonzalez-Gutierrez J, Sapkota J, Schuschnigg S, Holzer C (2018) Effect of the printing bed temperature on the adhesion of parts produced by fused filament fabrication. Plast Rubber Compos 47:17–24
18. Su R, Zhang Z, Love BJ, Shih AJ (2023) Fused filament fabrication of Nylon beyond the glass transition temperature in a thermally-insulated machine, Manuf Lett 35:797–804
19. Aliheidari N, Tripuraneni R, Ameli A, Nadimpalli S (2017) Fracture resistance measurement of fused deposition modeling 3D printed polymers. Polym Testing 60(94–101):0142–9418
20. Young D, Wetmore N, Czabaj M (2018) Interlayer fracture toughness of additively manufactured unreinforced and carbon-fiber-reinforced acrylonitrile butadiene styrene. Addit Manuf 22(508–515):2214–8604
21. Fonseca J, Ferreira I, De Moura M, Machado M, Alves J (2019) Study of the interlaminar fracture under mode I loading on FFF printed parts. Compos Struct 214(316–324):0263–8223
22. Barile C, Casavola C, Cazzato A (2018) Acoustic emissions in 3D printed parts under mode I delamination test. Materials 11(1760):1996–1944
23. Khudiakova A, Arbeiter F, Spoerk M, Wolfahrt M, Godec D, Pinter G (2019) Inter-layer bonding characterisation between materials with different degrees of stiffness processed by fused filament fabrication. Addit Manuf 28(184–193):2214–8604
24. Marșavina L, Stoia DI, Emanoil L (2021) Fracture toughness in additive manufacturing by selective laser sintering: an overview. Mater Des Process Commun 3(e254):2577–6576
25. Santos JD, Fernández A, Ripoll L, Blanco N (2022) Experimental characterization and analysis of the in-plane elastic properties and interlaminar fracture toughness of a 3D-printed continuous carbon fiber-reinforced composite. Polymers 14(506):2073–4360
26. Hart KR, Dunn RM, Sietins JM, Mock CMH, Mackay ME, Wetzel ED (2018) Increased fracture toughness of additively manufactured amorphous thermoplastics via thermal annealing. Polymer 144(192–204):0032–3861
27. Stamopoulos AG, Ilaria Scipioni S, Lambiase F (2023) Experimental characterization of the interlayer fracture toughness of FDM components. Compos Struct 320(3–4):117213
28. Northcutt LA, Orski SV, Migler KB, Kotula AP (2018) Effect of processing conditions on crystallization kinetics during materials extrusion additive manufacturing. Polymer 154. https://doi.org/10.1016/j.polymer.2018.09.018
29. Peng F, Vogt BD, Cakmak M (2018) Complex flow and temperature history during melt extrusion in material extrusion additive manufacturing. Additive Manuf 22:197–206
30. Foglia F, De Meo A, Iozzino V, Volpe V, Pantani R (2020) Isothermal crystallization of PLA: nucleation density and growth rates of α and α' phases. Can J Chem Eng 98:1998–2007
31. Volpe V, Foglia F, Pantani R (2020) Effect of the application of low shear rates on the crystallization kinetics of PLA. Polymer Crystal 3:e10139. https://doi.org/10.1002/pcr2.10139